Journal of Power Sources 427 (2019) 101–111

Contents lists available at ScienceDirect

Journal of Power Sources

journal homepage: www.elsevier.com/locate/jpowsour

Towards better estimability of electrode-specific state of health: Decoding the cell expansion

Peyman Mohtat*, Suhak Lee, Jason B. Siegel, Anna G. Stefanopoulou

Mechanical Engineering Department, The University of Michigan, Ann Arbor, MI, 48109-2125, USA

HIGHLIGHTS

- Monitoring the graphite lithiation state is essential for reducing lithium plating.
- Expansion improves the identifiability of graphite lithiation state.
- With expansion measurement, DOD required for observability is reduced to 30%.

GRAPHICAL ABSTRACT

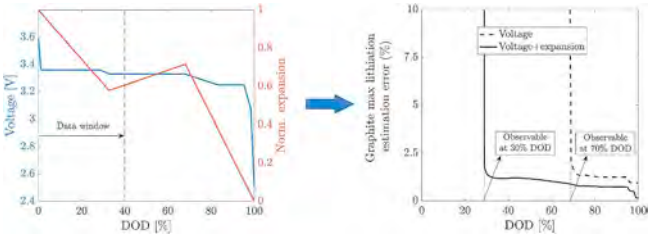

ARTICLE INFO

Keywords:
Li-ion batteries
Electrode state of health
Mechanical response
Identifiability analysis

ABSTRACT

Li-ion batteries are prone to adverse physical and chemical mechanisms that can degrade their performance over time. For this reason, identifying each electrode's capacity and utilization window is important for the safe operation of the battery, unfortunately the standard capacity estimation method cannot provide this. In this work, we introduce electrode-specific State of Health (eSOH) related parameters, including individual electrode capacity and utilization window. We explore the identifiability of the parameters using terminal voltage alone and voltage plus cell expansion measurements. The analysis here is based on the constrained Cramer-Rao Bound (CRB) formulation, which provides the error bounds for the parameters. The model utilizes the voltage/expansion functions of lithium stoichiometry for the individual electrodes based on the underlying physics of phase transitions. It is shown that slope changes in voltage and expansion that correspond to phase transitions in the electrodes enhance the estimation. As a result, with the addition of the expansion, the parameters are estimable without the need to discharge the battery to a high Depth of Discharge (>70%), which rarely happens in automotive applications. This makes eSOH estimation feasible for a wider range of real-world driving scenarios.

1. Introduction

The automotive industry is currently in a transition from conventional internal combustion power-train systems, to electrified power-train systems, powered by large battery packs with hundreds of cells. To keep the momentum of this transition going, it is paramount to have an advanced diagnostic and fault detection system available to alleviate safety and performance concerns. Furthermore, there is an increased interest in considering a second life for such batteries as energy storage on the larger electrical grid. To this end, we need to continuously monitor the electrode-specific State of Health (eSOH) of these batteries and to use them efficiently and safely with advanced battery management systems [1].

Li-ion batteries are sensitive to adverse physical and chemical conditions, which cause degradation of the battery performance. It is essential that we sense and avoid when these critical mechanisms are triggered through proper battery management. Currently, the battery state of health (SOH) is estimated by determining capacity (cyclable

* Corresponding author.
E-mail addresses: pmohtat@umich.edu (P. Mohtat), suhaklee@umich.edu (S. Lee), siegeljb@umich.edu (J.B. Siegel), annastef@umich.edu (A.G. Stefanopoulou).

https://doi.org/10.1016/j.jpowsour.2019.03.104
Received 10 January 2019; Received in revised form 22 February 2019; Accepted 25 March 2019
Available online 24 April 2019
0378-7753/

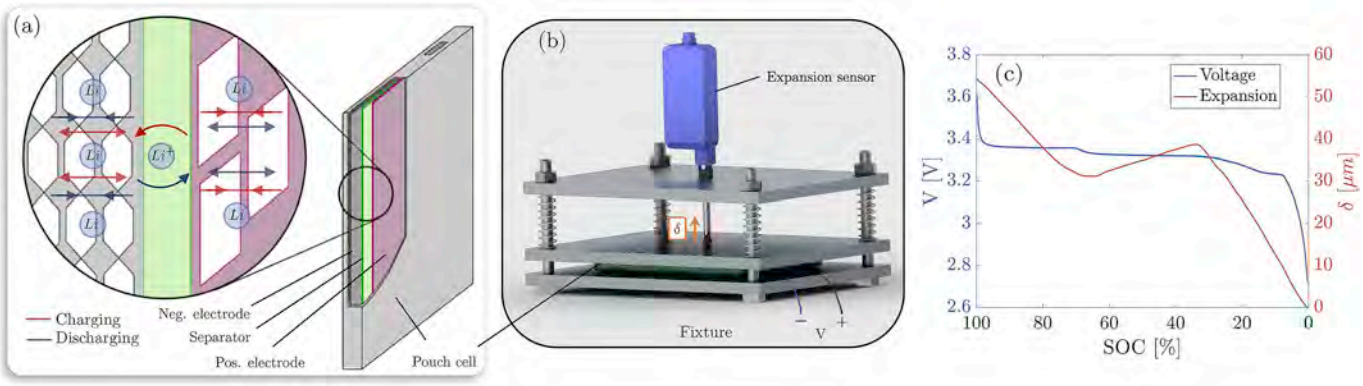

Fig. 1. (a) The schematic drawing of the inner working of a Li-ion battery. (b) The experimental setup, and (c) the voltage and expansion result of an LFP cell vs. state of charge (SOC) at a low c-rate.

energy) and cell resistance (power capability). This capacity is defined by the coulombs (=Amperes*time) that can be provided by a battery while operating within an acceptable voltage range. Many studies are concerned with estimating the battery's capacity without the need for a full discharge [2]. These methods estimate capacity by measuring voltage, current, and temperature. However, voltage limits alone may not be adequate for managing a battery safely since the limits may come from the anode SOH during charging and the cathode SOH during discharging. For example, irreversible lithium plating, which usually happens at low temperatures or during fast charging, causes Loss of Lithium Inventory (LLI) [3] and reduction of the battery's over all available capacity. The propensity of lithium plating is directly connected to the lithiation state of graphite at the end of a charge. Lithium plating is also a major safety risk as it may lead to an internal short circuit resulting in fire or even an explosion. Hence, this is also a safety limit coming from the anode SOH that needs to be considered. There are a number of studies that identify aging mechanisms using an underlying model with voltage and current measurements [4–7]. However, it has been shown that these aging mechanisms are only weakly detectable using terminal voltage-based estimation [8,9].

Another interesting and important type of battery response is the mechanical response. Batteries expand during charging and contract while discharging. For example, Fig. 1 (c) shows the expansion of a cell with lithium iron phosphate (LFP) chemistry during discharge at low C-rates. This expansion can be characterized either as a strain or stress. It has been shown that these stress/strain measurements can also be used for estimating the available capacity of the battery [10,11]. Although the idea of using stress/strain measurements to identify aging mechanisms, such as lithium plating [12], has been proposed, questions remain on the usefulness of this measurement. For example, given the fundamental relationship between voltage and strain [13], does this stress/strain give additional information about the battery's state of health that is not available in voltage?. Furthermore, is using stress/strain beneficial, given limits on data availability and sensor noise, for observability of the aging mechanisms?

The goal here is to explore the fundamental benefits of incorporating cell expansion measurements for estimating eSOH under noisy signals and limited data range. In this paper, the individual electrode capacity and utilization window are proposed as parameters related to eSOH. Furthermore, the relationship between these parameters and aging mechanisms are considered together. It is necessary to understand the usefulness of expansion before considering other difficulties associated with instrumenting cells in a pack. Hence, the model is developed using several simplifying assumptions; namely, that the effects of temperature and hysteresis on voltage and expansion are omitted. In addition, to have a better connection to the underlying physics, fundamental electrode potential and expansion functions have been developed and included in the model. The methodology for identifiability analysis is based on the Fisher information matrix that yields the Cramer-Rao bound for the estimation of eSOH parameters. Finally, the results for voltage only and voltage plus expansion measurements are obtained and compared.

The paper is organized as follows; Section 2 describes the experimental method. Section 3 introduces eSOH parameters and their connection to the aging mechanisms, the model for the voltage, and expansion of a cell. Section 4 introduces the physics-based electrode potential and particle level expansion. Section 5 presents the estimation problem, identifiability analysis methodology, and the virtual model of an LFP cell. Section 6 discusses the identifiability of parameters concerning the measurements. Section 7 summarizes the contributions.

2. Experimental method

The details of the pouch cell (A123) used in this work is shown in Table 3. The chemistry of the pouch cell was graphite/LFP. The experimental setup is shown in Fig. 1(b). The fixture was designed such that the top and bottom plates are fixed in place while the middle plate is free moving. To avoid the non-uniformities in the expansion, the fixture applied a small pressure on the pouch cell, by using compression springs. The applied pressure was around one psi given the spring constant and displacement. Also, the spring constants were much lower than the modulus of the cell [14]. Hence, the free movement of the middle plate with the addition of these springs allowed for more uniform free expansion of the pouch cell. The expansion was measured using a displacement sensor (Keyence, Japan) mounted on the top plate. The dynamic testing was carried using a battery cycler (Biologic, France). The temperature was measured using a K-type thermocouple (Omega, USA) place on the surface of the battery.

The fixture was installed inside a climate chamber with the temperature set to 25^oC. Then the cell was cycled 10 times at C/3 between 2.5 V and 3.6 V to ensure the repeatability of the expansion data. The cell was charged with a constant current (CC) from the fully discharged state at a low rate (C/20) to 3.6 V, followed by a constant voltage (CV) period until the current dropped below C/40, followed by a pause of 3 h. Then, the cell was discharged to 2.5 V at the same constant current. The cycle was repeated three times, and the measurements from the last cycle were reported.

3. Model development

3.1. Battery fundamentals

In a typical Li-ion battery, the porous electrodes consist of active material, in the form of particles, and a polymeric binder. The electrodes are attached to current collectors. Furthermore, the separator is a porous polymer, and the cell is filled up with the electrolyte.

In the discharging process lithium ions oxidized at the positive electrode (cathode) and reduced at the negative electrode (anode). The term cathode and anode is the electrode where oxidation and reduction happens, respectively. However, this takes place reversely while charging; the positive electrode is the anode, and the negative electrode is the cathode. Therefore, to avoid confusion in this paper, the terms negative and positive electrode are used.

For a Li-ion battery with graphite as the negative electrode and lithium iron phosphate (metal oxide) as the positive electrode, while the cell is charging or discharging the following chemical reactions take place at the negative and positive electrodes, respectively

$$Li_xC_6 \underset{c}{\overset{d}{\rightleftharpoons}} xLi^+ + xe^- + C6$$

$$Li_yFePO_4 + (1-y)Li^+ + (1-y)e^- \underset{c}{\overset{d}{\rightleftharpoons}} LiFePO_4,$$

where the forward direction indicates the discharging reactions and the backward direction indicates the charging reactions. This process is depicted in Fig. 1(a) with the red (blue) arrow denoting the charging (discharging) and expansion (contraction) of the lattice structure. The stoichiometric state x and y represent the degree of lithiation of each electrode. For example, the fully lithiated state of the graphite is $x = 1$ for Li_xC_6; i.e., one lithium atom per six carbon atoms.

3.2. Aging mechanisms and eSOH

To maximize the usage without inducing further degradation, estimating the type of degradation and state of health of the individual electrodes is required. There are a number of important degradation mechanisms for lithium-ion batteries. Solid Electrolyte Interphase (SEI) growth and lithium plating consume the reversible lithium during cycling leading to capacity fade. Other important mechanisms are structural disordering, metal dissolution, the loss of electrical contact, particle cracking, and blockage of active materials by the resistive surface film all leading to active material of the electrode becoming unavailable for insertion and extraction of lithium, and ultimately capacity reduction [6,9].

Due to a complex inter-correlations of these degradation mechanisms, it is extremely challenging to develop a diagnostic algorithm to capture all of them in the cell. However, it is possible to separate the effects of the mechanisms into two general modes of Loss of Lithium Inventory (LLI) and Loss of Active Material (LAM) at the positive and negative electrodes. Dubarry et al. [3], further categorized LAM under the consideration of the lithiated or delithiated state of LAM i.e. LAM_{liPE}, LAM_{dePE}, LAM_{liNE}, and LAM_{deNE}. Furthermore, LLI is also divided into two subcategories during; (1) charging in the negative electrode, and (2) discharging in the positive electrode. As a result of these aging mechanisms the utilization window and available capacity of each electrode changes. Hence, identifying the changes in individual electrode capacity and the associated shift of utilization window is important and informs the Battery Management System (BMS) about the aging mechanisms and electrode-specific constraints.

The importance of eSOH estimation is clarified in Fig. 2, using a simulated aging scenario for a graphite/LFP cell. The aging scenario corresponds to LAM_{deNE} mode, and the methodology presented in Ref. [3] is followed when producing this figure. In this mode, the negative electrode capacity is reduced by a significant amount, which is shown by the scaling of the negative potential denoted by purple arrows. At fresh and aged states, the cell operates between the same voltage limits defined as the safe range. However, for the aged state, the utilization of graphite electrode has shifted (denoted by a green arrow) to the dangerous region of low potential which increases the risk of lithium plating (marked by a dashed red area at the bottom of graphite half-cell potential). Furthermore, it is also evident that the shift of negative electrode operation window to a low potential is obscured in the terminal voltage. In contrast, Fig. 3 shows the effects of the same aging mechanism for the expansion of a single cell, where it suggests an observable change in the expansion of the fresh and aged cell.

In the following sections, the lithiation state of each electrode (utilization window) and the amount of available active material in each electrode (individual capacity) are introduced as eSOH parameters, using OCV and expansion. Furthermore, the equations connecting these parameters and aging mechanisms are discussed.

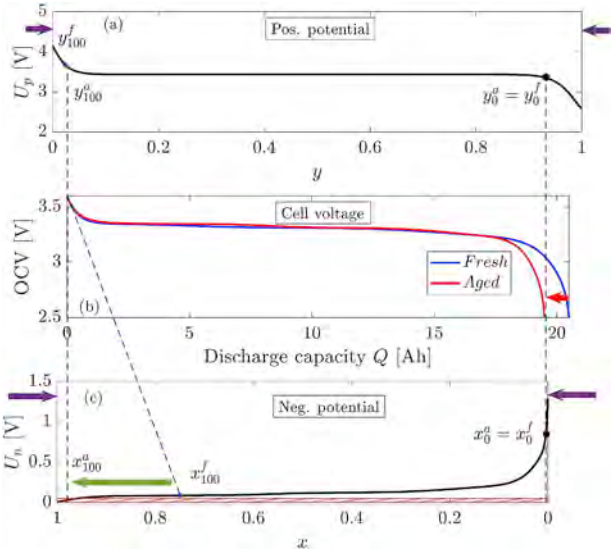

Fig. 2. (a) The half-cell potential of the positive electrode. (b) The Open Circuit Voltage (OCV) of a graphite/LFP cell at two states of life; fresh (blue) and aged (red), and (c) the negative electrode with corresponding utilization window at fresh (f) and aged (a) states. The simulated degradation correspond to 28% negative electrode capacity loss which corresponds to only 5% capacity fade for aged state of cell (middle) but forces the utilization window of the negative electrode deeply in the dangerous zone of lithium plating (bottom). (For interpretation of the references to colour in this figure legend, the reader is referred to the Web version of this article.)

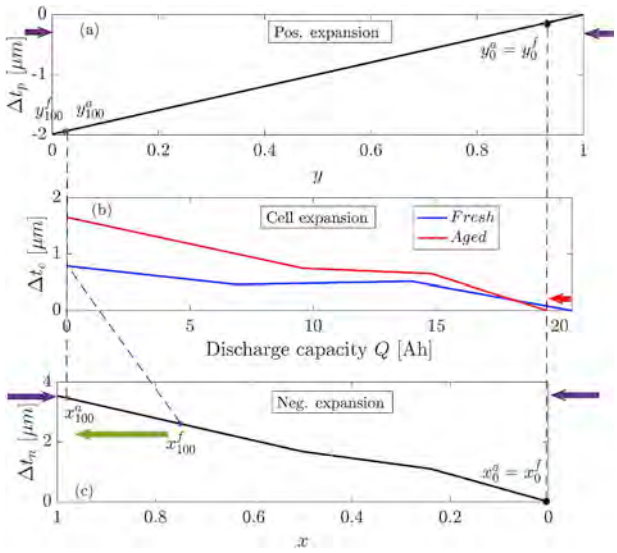

Fig. 3. (a) The half-cell expansion of the positive electrode. (b) The expansion of a graphite/LFP cell at two states of life; fresh (blue) and aged (red), and (c) the negative electrode with corresponding utilization window at fresh (f) and aged (a) states. The simulated degradation corresponds to 28% negative electrode capacity loss which corresponds to 5% capacity fade for the aged state of the cell. The figure suggests an observable change in the expansion of the fresh and aged cell. (For interpretation of the references to colour in this figure legend, the reader is referred to the Web version of this article.)

3.2.1. Open Circuit Voltage (OCV)

The OCV is the terminal voltage of a cell with no current flow, which can be written as the electrical potential difference between the positive and the negative electrodes. Let the potentials of the positive and negative electrode, measured against lithium, as a function of y and x, be denoted by (U_p) and (U_n), respectively. Then, while the cell is at an electrical equilibrium (no current is drawn and the voltage is at steady state), the terminal voltage of the cell is equal to Open Circuit Voltage (OCV) and satisfies the following

$$OCV(z) = U_p(y) - U_n(x), \tag{1}$$

where z is the depth of discharge (DOD) of the cell ($z = 1 - SOC$) and x, y are the *stoichiometric state* of negative and positive electrodes, receptively.

To prevent rapid cell degradation or power depletion, x and y are not necessarily from 0 to 1 for practical cells. Hence, the term *utilization window* is introduced for each electrode to represent the actual stoichiometric range used in each electrode. The utilization window is defined using the voltage limits specified for the battery, hence

$$U_p(y_0) - U_n(x_0) = V_{min}, \tag{2}$$

$$U_p(y_{100}) - U_n(x_{100}) = V_{max}. \tag{3}$$

where 100 and 0 subscripts denote the lithiation state of electrodes at two voltage limits V_{max}, and V_{min}, respectively.

Furthermore, the stoichiometric state of each electrode, $(x,\ y)$ satisfies the following relationship

$$z = \frac{Q}{C} = \frac{y - y_{100}}{y_0 - y_{100}} = \frac{x_{100} - x}{x_{100} - x_0}, \tag{4}$$

where Q is the coulomb counting from the charged state and C denotes the maximum capacity of the cell. With respect to the amount of available active material in each electrode the following equality holds

$$C = C_p(y_0 - y_{100}) = C_n(x_{100} - x_0), \tag{5}$$

where C_p and C_n denote the capacity of the positive and negative electrode in Amp-hours, respectively. These capacities correspond to the amount of active material in each electrode. Using Eq. (5), and Eq. (4) results in the following

$$z = \frac{Q}{C} = C_p\frac{y - y_{100}}{C} = C_n\frac{x_{100} - x}{C}. \tag{6}$$

Then, the individual stoichiometric states can be written as

$$y = y_{100} + \frac{Q}{C_p},\quad x = x_{100} - \frac{Q}{C_n}. \tag{7}$$

therefore, the half-cell potentials can be written as the function of the coulomb counting Q with the individual electrode parameters $(x_{100},\ y_{100},\ C_n,\ C_p)$

$$\begin{aligned} U_p(y) &= U_p\left(y_{100} + \tfrac{Q}{C_p}\right),\\ U_n(x) &= U_n\left(x_{100} - \tfrac{Q}{C_n}\right). \end{aligned} \tag{8}$$

Finally, Eq. (1) can be written as

$$OCV = U_p\left(y_{100} + \frac{Q}{C_p}\right) - U_n\left(x_{100} - \frac{Q}{C_n}\right). \tag{9}$$

The eSOH parameters are utilization window at charged state and capacity, $(x_{100},\ C_n)$ and $(y_{100},\ C_p)$, for negative and positive electrode, respectively.

3.2.2. Cell expansion

At any given moment in time, the thickness of the cell is the sum of thicknesses of its components. Similar to open circuit potential, the thickness of the electrodes can also be measured as a function of stoichiometric state at the open circuit state. Therefore, the thickness of the cell can be written as

$$t_c = n_c[t_p(y) + t_n(x)] + t_{ic}^0, \tag{10}$$

where $t_n(x)$ and $t_p(y)$ are functions denoting the thickness of the negative and the positive electrode, n_c is the number of parallel cells stacked on top of each other in the battery, and t_{ic}^0 is the total thickness of inactive components (i.e. current collectors, separator, etc.), which in the case of free expansion is assumed to be constant.

The porous electrode, in addition to the active material, has embedded binder polymer, furthermore, the electrode is glued to the current collector whereas it has free movement on the separator side. This makes the process of going from particle to electrode expansion complicated. To simplify this process it is assumed first that because of the large electrode length to thickness ratio and high stiffness, the electrode only expands in the through-plane direction. Second, the changes in electrode thickness come only from the active material and contribution of binder and other add-ons are not considered. Following the results from Ref. [15] with the same set of assumptions, an ample estimate of the electrode expansion can be calculated by

$$\Delta t_i = \xi_i t_i^0 \Delta\mathscr{V}_i. \tag{11}$$

where subscript i is either p or n for respected electrode, ξ is the volume fraction of active material in the electrode, t^0 is the initial thickness of the electrode. Furthermore, $(\Delta\mathscr{V}_p)$ and $(\Delta\mathscr{V}_n)$ denote the changes in volume at particle level as a volumetric strain. The volumetric strain is a function of the stoichiometric state y for the positive electrode and x for the negative electrode.

Using Eq. (11), the thickness of the battery can be written as

$$t_c = n_c\left[(1 + \xi_p\Delta\mathscr{V}_p(y))t_p^0 + (1 + \xi_n\Delta\mathscr{V}_n(x))t_n^0\right] + t_{ic}^0, \tag{12}$$

where t_n^0 and t_p^0 are the thickness of the negative and the positive electrode at the fully discharged state of the cell.

Following the same procedures of the previous section, the stoichiometric states $(x,\ y)$ are substituted using Eq. (7). As a result, the equation for thickness is

$$\begin{aligned} t_c = n_c\Bigg[&\left(1 + \xi_p\Delta\mathscr{V}_p\left(y_{100} + \frac{Q}{C_p}\right)\right)t_p^0 + \left(1 + \xi_n\Delta\mathscr{V}_n\left(x_{100} - \frac{Q}{C_n}\right)\right)t_n^0\Bigg]\\ &+ t_{ic}^0. \end{aligned} \tag{13}$$

Often it is more practical to measure the expansion using a displacement sensor rather than the total thickness of the battery. Therefore, it is also necessary to define an initial set point to calculate the expansion. In application, batteries rarely go to the fully discharged state, hence for convenience the expansion is assumed to be measured with respect to the fully charged state. Hence the expansion is written as

$$\Delta t_c = t_c^{100} - t_c, \tag{14}$$

where t_c^{100} is thickness of the battery at fully charged state.

Finally, using Eq. (13) the cell expansion is as follows

$$\begin{aligned} \Delta t_c = n_c\Bigg[&\left(\Delta\mathscr{V}_p(y_{100}) - \Delta\mathscr{V}_p\left(y_{100} + \frac{Q}{C_p}\right)\right)\xi_p t_p^0\\ &+ \left(\Delta\mathscr{V}_n(x_{100}) - \Delta\mathscr{V}_n\left(x_{100} - \frac{Q}{C_n}\right)\right)\xi_n t_n^0\Bigg], \end{aligned} \tag{15}$$

where the first term inside each parenthesis is coming from the thickness of the cell at the fully charged state.

3.2.3. Aging mechanisms diagnostics

With eSOH parameters defined in the previous sections, it is now possible to introduce the equations describing the amount of different aging mechanisms. The percentage amount of LAM in each electrode, is

the reduction in available individual electrode capacity (C_p, C_n) and its given by

$$LAM_{pe}\ \%= \left(1 - \frac{C_p^a}{C_p^f}\right) \times 100,$$
$$LAM_{ne}\ \%= \left(1 - \frac{C_n^a}{C_n^f}\right) \times 100, \tag{16}$$

where the superscript f and a denote the fresh and aged state, respectively. Note that the LAM here is the overall amount of LAM of lithiation and delitiation. The amount of intercalated lithium in the electrode at any SOC is given by the following

$$n_{Li} = \frac{3600}{F}(yC_p + xC_n), \tag{17}$$

where F is the Faraday constant. It is straight-forward to show that the above amount is constant, assuming lithium conservation,

$$\frac{3600}{F}\left(\left(y + \frac{\Delta Q}{C_p}\right)C_p + \left(x - \frac{\Delta Q}{C_n}\right)C_n\right) = \frac{3600}{F}(yC_p + xC_n), \tag{18}$$

where ΔQ denotes discharging in Amp-hours. Hence, the n_{Li} can be calculated with respect to fully charged state

$$n_{Li} = \frac{3600}{F}(y_{100}C_p + x_{100}C_n). \tag{19}$$

Finally, the LLI is defined as the percentage reduction in the above amount

$$LLI\ \%= \left(1 - \frac{n_{Li}^a}{n_{Li}^f}\right) \times 100, \tag{20}$$

where the superscript f and a denote the fresh and aged state, respectively. LLI here denotes the total loss of lithium.

4. Materials with phase transitions

In this section, fundamental models of electrode potential (U_p, U_n), and particle level expansion ($\Delta\hat{\varepsilon}_p$, $\Delta\hat{\varepsilon}_n$) are presented. The potential is represented by approximations of the thermodynamic equilibrium potentials of the porous electrodes [16]. Furthermore, the expansion is represented by associating the expansion to the changes in lattice parameters during charge/discharge. In section 5, it will be shown that the sensitivity matrix of OCV and expansion to the parameters is related to the slope of each electrode potential and expansion. In the following, the connection between these slopes and the phase transitions of electrode material is explained for the graphite/LFP chemistry.

4.1. A fundamental model of the potential

A number of materials used as insertion electrode in Li-ion cells undergo different phase transitions during lithium (de)intercalation, and the potential displays several plateaus with fast changes between them, which results in the so-called “staircase” voltage curve [17]. The plateaus correspond to the coexistence of Li-rich and Li-poor regions, where the two phases do not mix, hence the material *phase separate* into the two regions. Furthermore, the steps between the plateaus denote the boundary in which the phase transition completes.

In this study, a cell consisting of a graphite electrode and lithium iron phosphate (LFP) electrode is considered. Both of these materials display the phase separating characteristic; LFP with one vast plateau and graphite with several plateaus.

Positive electrode: Lithium iron phosphate is a cathode material gaining popularity due to its safety, low cost and relatively high rate capability and long cycle life [18]. It has a vast voltage plateau which corresponds to a strong tendency of the material to phase separate.

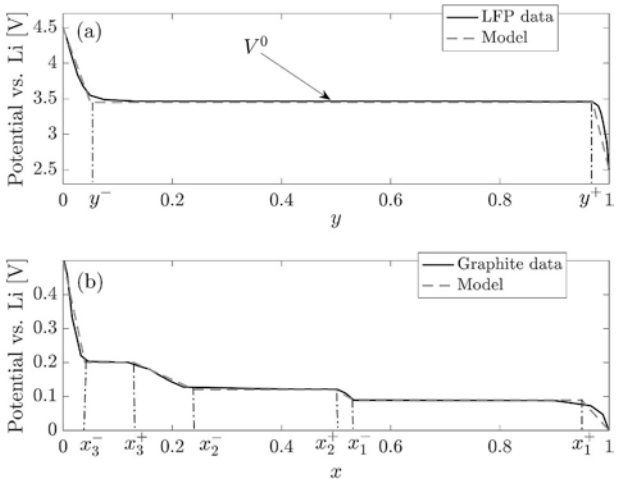

Fig. 4. (a) The potential (solid-line) of Li_yFePO_4 [20] and its piecewise linear approximation (dashed-line). Furthermore, the potential at $y = 0.5$ is denoted by V^0, and plateau section is bounded by (y^-, y^+). (b) The potential (solid-line) of Li_xC_6 [19] and its piecewise linear approximation (dashed-line).

A simple thermodynamical model of a phase separating material is the regular solution of particles and vacancies [16]. The equation describing the chemical potential is

$$\mu(y) = \frac{\Omega}{2}(0.5 - y) + k_BTln\left(\frac{y}{1-y}\right), \tag{21}$$

where Ω is the regular solution interaction parameter, k_B is the Boltzmann's constant, and T is the absolute temperature. Then the open circuit potential, U_p, measured against lithium metal as reference potential is simply,

$$U_p(y) = V^0 + \frac{\Omega}{2e}(y - 0.5) - \frac{k_BT}{e}ln\left(\frac{y}{1-y}\right), \tag{22}$$

where V^0 is standard potential, and e is the charge of an electron. This equation also shows that $U_p(0.5) = V^0$. For $\Omega > 2k_BT$ the material is phase separating and the chemical potential is non-monotonic. However, the actual voltage measurement is monotonic with a large flat section called the miscibility region, which is bounded by (y^-, y^+). This voltage behavior has been modeled using a multiple particle approach, which also models the voltage hysteresis of LFP. For further discussion on this subject the reader is referred to Refs. [16,21]. The values of the bound can be find by setting the chemical potential to zero. Fig. 4(a) shows the potential response and the concentrations bounding the plateau for LFP. Here the two phases are $FePO_4$ and $LiFePO_4$.

Inspired by the above model, a piecewise linear approximation of the potential of two phase materials (e.g. LFP) is developed. The steps are as follows:

1 The potential at the center of the plateau region, V^0, is identified (Table 1).
2 The concentrations bounding the plateau (y^-, y^+) are chosen empirically (Fig. 4(a)).
3 A line is constructed on the plateau intersecting with V^0 in the (y^-, y^+) region.
4 A second line is constructed for the initial potential drop using the starting point of data, (U_p, y) = (U_{max}, 0) (voltage range), and point y^- of the plateau line.

Table 1
The different phase coexistences with their plateau potential and approximate range for graphite [19] and LFP [20].

Electrode material	Phase coexistence	x, y range	V^0 (V)
LFP			
	$FePO_4$ & $LiFePO_4$	$0 \le y \le 1.0$	3.45
Graphite (C)			
	Dilute 1 & Stage 4	$0 \le x < 0.13$	0.2
	Stage 4 & Stage 3	$0.13 \le x < 0.24$	–
	Stage 3 & Stage 2	$0.24 \le x < 0.5$	0.12
	Stage 2 & Stage 1	$0.5 \le x \le 1.0$	0.09

5 A third line is constructed for the end potential drop using the ending point of data, $(U_p,\ y) = (U_{min},\ 1)$ (voltage range), and point y^+ of the plateau line.

Using this methodology and data from Ref. [20], the following potential function is obtained

$$U_p(y)\,[V] = \begin{cases} -20.99y + 4.5 & y < 0.05 \\ -7 \times 10^{-6}(y - 0.5) + 3.45 & 0.05 \le y < 0.97 \\ -31.66y + 34.16 & 0.97 \le y. \end{cases} \quad (23)$$

In this function the plateau boundary is $(y^-,\ y^+) = (0.05,\ 0.97)$, midpoint potential is $V^0 = 3.45\,[V]$, and potential range is $(U_{min},\ U_{max}) = (2.5,\ 4.5)\,[V]$. The piecewise linear approximation and data from Ref. [20] are depicted in Fig. 4(a).

Negative electrode: The graphite is used extensively as anode material. It undergoes several phase transitions in its potential response [22]. In graphite, Li intercalates between graphene planes but prefers to populate isolated layers. Each *phase* correspond to a different filling order of lithium atoms between graphene layers called a *stage*. The stage number, n, is the number of graphene layers between layers of lithium atoms with every n^{th} layer Li-rich, and the other layers Li poor.

The stages are as follows: At the very low concentrations of lithium ($x < 0.04$), the lithium atoms are randomly distributed in the graphite, and there is no apparent structure, this stage is called a dilute stage 1. As the concentration increases a more structured phase, stage 4, begins to take shape. The plateau at 200 mV corresponds to dilute stage 1 and stage 4 phase transition. Next is the formation of stage 3, the transition from stage 4 to 3 happens in ($0.13 < x < 0.24$). Unlike others the phase transitions between these stages seem to be continuous, indicating a random mix of these two phases, hence there is no plateau corresponding to this phase transition. The next plateau at 120 mV corresponds to stage 3 and stage 2 phase transition. Finally is the development of the densest structure, stage 1, which is one layer of graphene between layers of lithium atoms. The plateau at 90 mV corresponds to stage 2 and stage 1 phase transition.

A summary of different phase transitions of graphite as well as the LFP is presented in Table 1, the potential of each plateau is also reported. A similar procedure to LFP is used to get a piecewise linear representation of the potential response of the graphite. The concentrations bounding the plateaus are indicated in Fig. 4(b). Furthermore, the potential range is $(U_{min},\ U_{max}) = (0, 0.5)\,[V]$. As indicated in Table 1, the stage 4 to 3 transition does not produce a plateau [19], therefore, is approximated with a line. Using this methodology and potential data for graphite from Ref. [19], the function used for approximating the potential is

$$U_n(x)\,[V] = \begin{cases} -7.46x + 0.5 & x < 0.04 \\ -0.008(x - 0.085) + 0.20 & 0.04 \le x < 0.13 \\ -0.71x + 0.2931 & 0.13 \le x < 0.24 \\ -0.005(x - 0.37) + 0.12 & 0.24 \le x < 0.50 \\ -0.94x + 0.5893 & 0.50 \le x < 0.53 \\ -0.005(x - 0.74) + 0.09 & 0.53 \le x < 0.95 \\ -1.77x + 1.77 & 0.95 \le x. \end{cases} \quad (24)$$

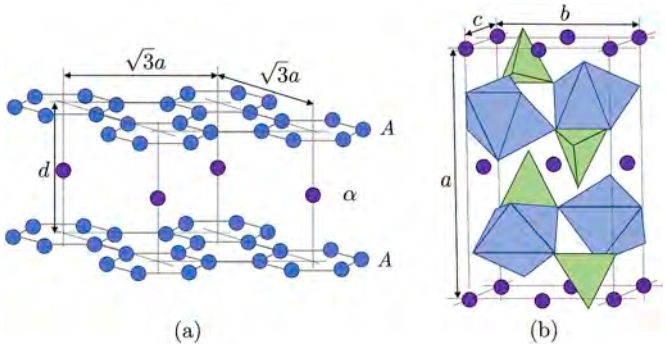

Fig. 5. (a) The crystal structure of LiC_6 (stage 1) with $A\alpha A$ stacking. The lithium atoms (represented by purple circles) are at the fictitious layer, α, midway the graphene layers [25]. (b) The crystal structure of $LiFePO_4$. The tetrahedra represent PO_4., and the octahedra represent FeO_6 [26]. (For interpretation of the references to colour in this figure legend, the reader is referred to the Web version of this article.)

The potential response of graphite and the piecewise linear approximation are depicted in Fig. 4(b).

4.2. A model for lattice volume changes

The intercalation of Li inside the electrode material induces dimension changes and internal stress generation of the electrode. Depending on the electrode material the volume changes could be as significant as 300% from the delithiated state [23], as in silicon. This expansion stems from the changes in lattice parameters and structure of the electrode while the concentration of Li increases in the electrode. Battery expansions can be measured either as thickness changes (free expansion) or as force (constrained expansion). Furthermore, it has been shown that using the expansion measurement helps in a number of scenarios relating to the state of charge and state of health estimation [10,24].

In order to model the expansion of the cell, it is possible to utilize the changes in the lattice structure. Graphite consists of layers of graphene in a hexagonal structure, and Li intercalates in the spaces between the layers. The distance between the layers is denoted by d, and the distance between the center of adjacent hexagons is denoted by a. In Fig. 5(a), the crystal structure of lithiated graphite is depicted. The unite lattice volume is a rhombohedron. Table 2 shows the edge length of the unit cell and average d-spacing for different phases of graphite. The changes in the volume are calculated using these values and included in Table 2. The changes of lattice parameters are anisotropic since the expansion of d is greater than a. However, at the particle level, the layers are orientated randomly. Hence the electrode material can be assumed to be isotropic. Thus, it is possible to utilize the changes in lattice parameters to calculate the volume changes in the particle.

The data reported in Table 2 are for the pure phases and between these states, the material is a mixture of two phases. Hence, it can be assumed that expansion evolves linearly between the two pure phases. This linear behavior is also observed in the experiment (see Fig. 1(c)). Using this assumption one can derive a piecewise linear function based on the available lattice data points. Hence, the function for volume changes of graphite is

$$\Delta\hat{\mathscr{V}}_n(x)\,[\%] = \begin{cases} 16.96x & x < 0.13 \\ 16.91(x - 0.3) + 2.20 & 0.13 \le x < 0.24 \\ 8.13(x - 0.2) + 4.06 & 0.24 \le x < 0.50 \\ 13.76(x - 0.5) + 6.18 & 0.5 \le x. \end{cases} \quad (25)$$

Similar steps can also be carried out for LFP to go from lattice expansion to particle expansion. The unit lattice volume for LFP is a rectangular cuboid. In Fig. 5(b), the crystal structure of LFP is depicted. The volume change is calculated with respect to the fully lithiated state

Table 2
Unit cell lattice parameters, unit cell volume, and percentage changes in volume for different phases of graphite and LFP [19,25,26].

Material	Phase	Structure	x, y	Unit lattice parameters (Å)			Unit lattice volume (Å^3)	$\Delta\mathscr{V}$ (%)
LFP				a	b	c	$\mathscr{V} = abc$	
	$LiFePO_4$	orthorhombic	1.00	10.33	6.01	4.69	291.2	0
	$FePO_4$	orthorhombic	0.00	9.810	5.79	4.78	271.5	−6.76
Graphite				$\sqrt{3}a$		d	$\mathscr{V} = \frac{3\sqrt{3}a^2}{2}d$	
	C	hexagonal	0	4.239		3.35	52.13	0
	Stage 4	hexagonal	0.13	4.254		3.40	53.28	2.20
	Stage 3	hexagonal	0.24	4.255		3.46	54.25	4.06
	Stage 2	hexagonal	0.50	4.262		3.51	55.35	6.18
	Stage 1	hexagonal	1.00	4.289		3.70	58.94	13.06

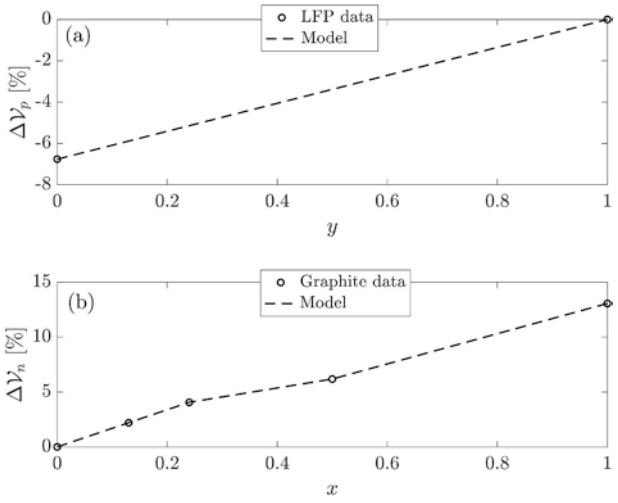

Fig. 6. The piecewise linear approximation functions for volume changes of particle for (a) LFP and (b) graphite along with the data from Table 2.

and is shown in Table 2. The piecewise linear function for volume changes of LFP is

$$\Delta\mathscr{V}_p(y)\,[\%] = -6.76(1-y). \tag{26}$$

The piecewise linear functions for the volume changes of the graphite and LFP are depicted in Fig. 6.

5. Parameter identification

In this section, a methodology to estimate the eSOH parameters, based on voltage and expansion measurements, is presented. Furthermore, the identifiability analysis for the parameters are discussed and to carry out the identifiability analysis, a virtual model based on piecewise linear functions is introduced.

5.1. Estimation problem

The parameters, $\theta = [x_{100},\ y_{100},\ C_n,\ C_p]$, related to electrode specific SOH can be estimated by solving the following problem using measurements at coulomb counting Q_i, terminal voltage at rest OCV_i, and cell expansion at rest Δt_{ci}

$$\min_{\theta} \sum_{i=1}^{N} \|Y(\theta, Q_i) - \hat{Y}_i\|^2. \qquad (P)$$

subject to, $U_p(y_{100}) - U_n(x_{100}) = V_{max}$,

where $Y(\theta, Q_i) = \begin{bmatrix} OCV(\theta, Q_i) \\ \Delta t_c(\theta, Q_i) \end{bmatrix}$, and vector of measurements is $\hat{Y}_i = \begin{bmatrix} OCV_i \\ \Delta t_{ci} \end{bmatrix}$. It is assumed that the cell operation is constrained between the same cell voltage limits in its lifetime. The voltage limits define the capacity and the utilization window of the cell (see Eqs. (2), and (3)). With a partial discharge scenario, the capacity of the cell is also unknown. Therefore, to focus the estimation on the eSOH parameters, the capacity is not included in the above formulation. Hence, only the maximum voltage limit is used in the estimation problem. Nevertheless, after finding θ, the capacity of the cell, C, can be estimated by solving the minimum voltage constraint equation given by

$$V_{min} = U_p\left(y_{100} + \frac{C}{C_p}\right) - U_n\left(x_{100} - \frac{C}{C_n}\right), \tag{27}$$

where Q in Eq. (9) is substituted with C.

5.2. Identifiability analysis

The identifiability analysis can be explored by means of Fisher Information Matrix (FIM), and the Cramer-Rao bound (CRB) matrix, which gives the lower bound on the error covariance matrix of an unbiased estimate of a nonrandom parameter vector. Problem (P) has an equality constraint related to the maximum voltage of the cell. Therefore, here a methodology based on [27] is introduced, which incorporates the equality constraints in the calculation of the CRB.

It is assumed that the measurements can be modeled as

$$\hat{Y} = Y(\theta) + \varepsilon, \tag{28}$$

where ε is an additive measurement error, which can include measurement noise and model mismatch. In the context of a least squares estimation problem, assuming a zero mean Gaussian vector with the covariance matrix, E, for ε, the FIM can be written as [28].

$$\mathscr{I}_f = S^T E^{-1} S, \tag{29}$$

where $S = \partial Y/\partial\theta$ is the local sensitivity matrix calculated at true $\theta = \theta^*$. If FIM is nonsingular, the $\mathscr{I}_f^{-1}$ is the *unconstrained* CRB for the error covariance matrix of θ.

Since the problem statement (P) has a constraint, following procedure is used to determine the *constrained* CRB [27]. Let the constraints be defined as follows

$$f(\theta^*) = 0, \tag{30}$$

where it is assumed that f is locally differentiable. Define $\mathscr{O}$ as an orthogonal matrix ($\mathscr{O}^T\mathscr{O} = I$), which forms an orthonormal basis for the nullspace of the gradient of the constraints. That is

$$\frac{\partial f(\theta)}{\partial\theta}|_{\theta^*}\mathscr{O} = 0. \tag{31}$$

If $\mathscr{O}^T\mathscr{I}_f\mathscr{O}$ is nonsingular, then the *constrained* problem is identifiable, moreover, the error covariance, Σ matrix i.e. *constrained* CRB is

$$\Sigma \geq \mathcal{O}(\mathcal{O}^T \mathcal{I}_f \mathcal{O})^{-1} \mathcal{O}^T. \tag{32}$$

Furthermore,

$$\sigma_\theta = \sqrt{diag[\Sigma]}, \tag{33}$$

where σ_θ is the standard parameter error. Furthermore, the standard error is normalized with respect to the parameters true value to give a percentage error as following:

$$Error\ (\%) = \frac{\sigma_{\theta_i}}{\theta_i} \times 100. \tag{34}$$

5.3. Slopes of electrode potential and expansion

Under the assumption that the noise is zero-mean Gaussian and independent, E can be written as

$$E = \begin{bmatrix} E_V & 0 \\ 0 & E_t \end{bmatrix}, \tag{35}$$

where $E_V = diag[\sigma_V^2]$ and $E_t = diag[\sigma_t^2]$. Furthermore, the sensitivity matrix, S, can be written as

$$S(\theta^*) = \begin{bmatrix} S_V(\theta^*) \\ S_t(\theta^*) \end{bmatrix}, \tag{36}$$

where $S_V = \frac{\partial OCV}{\partial \theta}|_{\theta^*}$, $S_t = \frac{\partial \Delta t_c}{\partial \theta}|_{\theta^*}$.

For the optimization problem (P) in this study, the sensitivity of OCV (Eq. (9)) with respect to x_{100} corresponds to the first column of $S_V(\theta^*)$. At measurement, Q_i, corresponding to stoichiometric state, x_i (Eq. (7)), this entry is as follows

$$\frac{\partial OCV_i}{\partial x_{100}} = \frac{\partial OCV_i}{\partial x_i} \cdot \frac{\partial x_i}{\partial x_{100}} = -\frac{\partial U_n}{\partial x_i}, \tag{37}$$

which is the slope of the negative electrode potential. The second column of $S_V(\theta^*)$ is computed as $\frac{\partial OCV_i}{\partial y_{100}} = \frac{\partial U_p}{\partial y_i}$ which is the slope of the positive electrode potential. The third and fourth column are calculated similarly. Then, the sensitivity matrix assuming N measurements with $Q_1, \ldots, Q_N$ charge levels can be written as

$$S_V(\theta^*) = \begin{bmatrix} -\frac{\partial U_n}{\partial x_1} & \frac{\partial U_p}{\partial y_1} & -\frac{\partial U_n}{\partial x_1}\frac{Q_1}{C_n^2} & -\frac{\partial U_p}{\partial y_1}\frac{Q_1}{C_p^2} \\ \vdots & \vdots & \vdots & \vdots \\ -\frac{\partial U_n}{\partial x_N} & \frac{\partial U_p}{\partial y_N} & -\frac{\partial U_n}{\partial x_N}\frac{Q_N}{C_n^2} & -\frac{\partial U_p}{\partial y_N}\frac{Q_N}{C_p^2} \end{bmatrix}. \tag{38}$$

For the case of voltage only measurements, if all the measurements are from a single slope the first and second columns in the sensitivity matrix in Eq. (38) become linearly dependent due to the same values of entries for all measurements. Thus, the sensitivity matrix is rank deficient and the problem is unidentifiable. Hence, at minimum the measurements have to be taken from regions with different slopes.

The sensitivity of expansion (Eq. (15)) to x_{100} is as follows

$$\begin{aligned} \frac{\partial \Delta t_{ci}}{\partial x_{100}} &= n_c \xi_n t_n^0 \left(\frac{\partial \Delta \hat{\gamma}_n}{\partial x_{100}}|_{x_{100}^*} - \frac{\partial \Delta \hat{\gamma}_n}{\partial x_i} \cdot \frac{\partial x_i}{\partial x_{100}} \right) \\ &= w_n \left(\gamma^{100} - \frac{\partial \Delta \hat{\gamma}_n}{\partial x_i} \right) \end{aligned}, \tag{39}$$

where $\gamma^{100} = \frac{\partial \Delta \hat{\gamma}_n}{\partial x_{100}}|_{x_{100}^*}$, and $w_n = n_c \xi_n t_n^0$ are substituted for brevity. The second column of $S_t(\theta^*)$ is computed as $\frac{\partial \Delta t_{ci}}{\partial y_{100}} = w_p \left(\zeta^{100} - \frac{\partial \Delta \hat{\gamma}_p}{\partial y_i} \right)$, where $\zeta^{100} = \frac{\partial \Delta \hat{\gamma}_p}{\partial y_{100}}|_{y_{100}^*}$, and $w_p = n_c \xi_n t_p^0$. The third and fourth column are calculated similarly. Then, the sensitivity matrix can be written as

Table 3
The parameters used in the virtual model for identifiability demonstration.

Pouch cell			
Nominal capacity		20.5 Ah	
Operating voltage		2.5–3.6 V	
		Graphite	LFP
Electrode thickness t_i^0 (μm)		43 [29]	70 [30]
Active material volume ration ξ_i		0.63 [29]	0.42 [30]
Electrode potential $U_i(V)$		Eq. (24)	Eq. (23)
Particle volume expansion $\Delta \hat{\gamma}_i$ (%)		Eq. (25)	Eq. (26)
Fitted parameters			
x_{100}	y_{100}	C_n (Ah)	C_p (Ah)
0.741	0.038	27.85	21.65

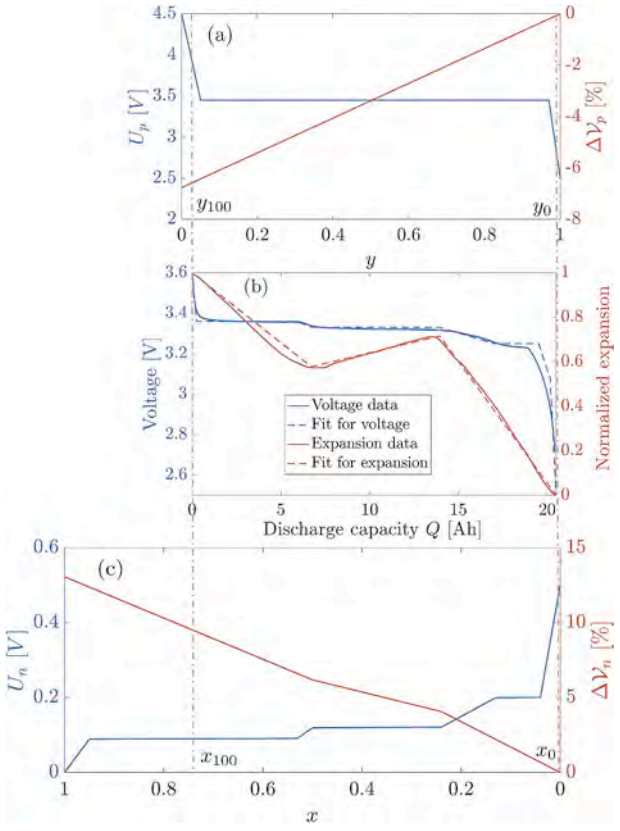

Fig. 7. (a) The model of potential and expansion of LFP, and (c) graphite. (b) The fitting results of OCV and expansion along with the data.

$$S_t(\theta^*) = \begin{bmatrix} w_n\left(\gamma^{100} - \frac{\partial \Delta \hat{\gamma}_n}{\partial x_1}\right) & w_p\left(\zeta^{100} - \frac{\partial \Delta \hat{\gamma}_p}{\partial y_1}\right) & -w_n \frac{\partial \Delta \hat{\gamma}_n}{\partial x_1}\frac{Q_1}{C_n^2} & w_p \frac{\partial \Delta \hat{\gamma}_p}{\partial y_1}\frac{Q_1}{C_p^2} \\ \vdots & \vdots & \vdots & \vdots \\ w_n\left(\gamma^{100} - \frac{\partial \Delta \hat{\gamma}_n}{\partial x_N}\right) & w_p\left(\zeta^{100} - \frac{\partial \Delta \hat{\gamma}_p}{\partial y_N}\right) & -w_n \frac{\partial \Delta \hat{\gamma}_n}{\partial x_N}\frac{Q_N}{C_n^2} & w_p \frac{\partial \Delta \hat{\gamma}_p}{\partial y_N}\frac{Q_N}{C_p^2} \end{bmatrix}. \tag{40}$$

Therefore the identifiability of the parameters in the estimation problem depends on the number of rate changes in electrode potential/expansion included in the measurement.

5.4. Graphite/LFP cell model

The eSOH parameters are fitted to the *full range* of voltage and expansion data. The fitting results are reported in Table 3. Furthermore,

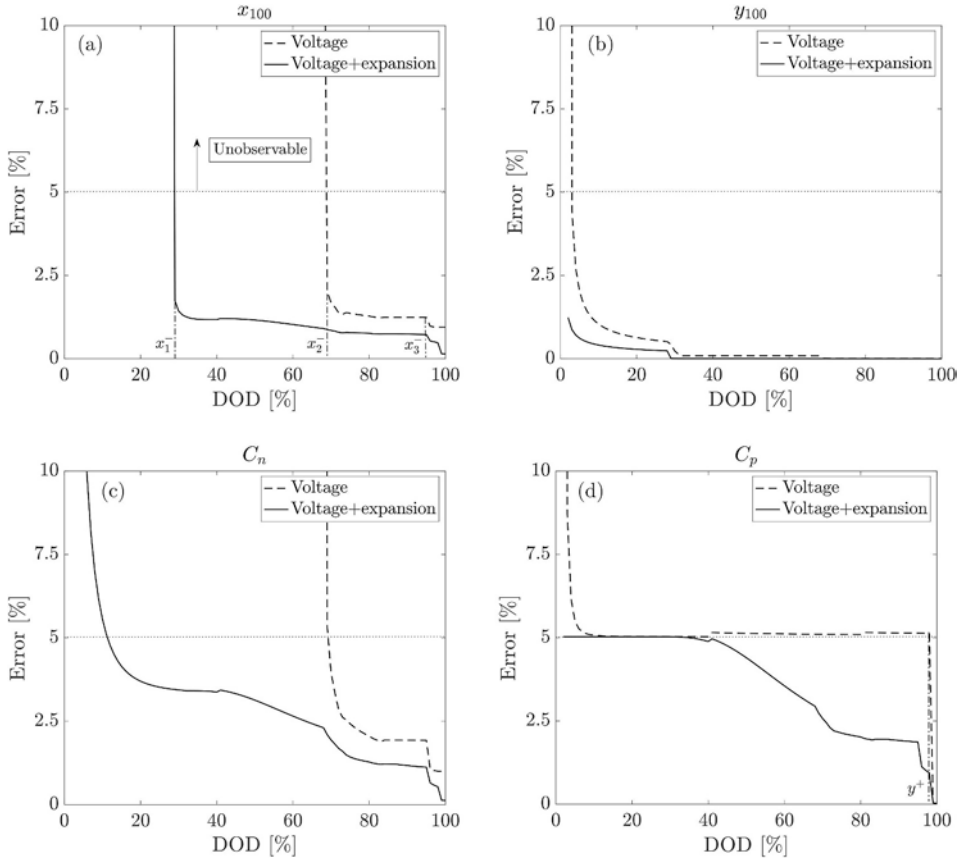

Fig. 8. Parameter error of (a) x_{100} (b) y_{100} (c) C_n (d) C_p calculated for different data windows starting from fully charge and ending at DOD, plotted for the case of voltage only and the case of voltage plus expansion measurements. The results show that the estimation error decreases substantially with the addition of expansion measurements compare to the case of voltage only measurements.

the data and the fitting result are shown in Fig. 7, which also shows the relationship between electrode potential/expansion and the cell voltage/expansion. In this figure, the expansion is normalized with respect to maximum expansion to show the characteristic behavior of a representative cell in the battery. Based on the fitting result, a virtual model is constructed to study the identifiability of the parameters under a variety of data availability scenarios, such as a limited number of measurements, and identifiability under voltage and voltage plus expansion measurements. The virtual model uses the piecewise linear functions introduced in Section 4.

6. Results and discussion

In this section, the result of identifiability analysis for eSOH parameters is presented and discussed. The analysis is done using the data generated by the virtual model. The limited data scenarios include a case of voltage measurements alone and a case of voltage plus expansion measurements, both with data available only in certain SOC windows. The data window is defined as follows: it is assumed that there is one measurement opportunity at every 1% change in SOC, starting from the fully charged state. With each addition of the measurements, the standard error of the parameters is calculated. The size of the data window is denoted by the depth of discharge (DOD). Given that the method so far relies on the open circuit state, for transportation applications, the data can accumulate every time there is an open circuit opportunity, for instance, at every key-on with ample rest time before it. Also, at very low c-rate such as level 1 charging.

The results of the standard parameter error versus the DOD (data window) are shown in Fig. 8. This result is obtained using $\sigma_V = 10\ mV$ and $\sigma_t = 5\ \mu m$ measurement error. The goal is to show the relative observability of the two scenarios of voltage alone and voltage plus expansion measurements. For this paper, the data window starts from the fully charged state. It is straight-forward to apply the same analysis for a data window starting at a lower SOC for voltage. However, since the expansion is defined with respect to the fully charged state (see Eq. (14)) and to be able to compare the two scenarios, only the data windows starting from the fully charged state are considered.

6.1. Connection to phase transitions

The results indicate that as the measurements move to a higher DOD, the estimation error decreases for all the parameters. This reduction happens in stages, which corresponds to the phase transitions in the material. For example, for the parameter x_{100}, the estimation error decreases as the graphite is transitioning from stage 1 to stage 4 (Tables 1 and 2). Each error reduction corresponds to the ending of a plateau (phase coexistence), which is indicated by bounding stoichiometric states (x_1^-, x_2^-, x_3^-) in the figure. For example, the first error reduction ($x \approx 0.5$) corresponds to slope changes in both voltage and expansion. Furthermore, for the parameter C_p, in case of voltage alone measurement, the estimation error remains at a constant value until almost 98% DOD, which corresponds to the stoichiometric state (y^+) bounding the plateau in LFP.

As shown in Eqs. (38), and (40), the identifiability of the parameters depends on rate changes of electrode voltage/expansion, which is related to phase transition in the material. Therefore, it is deduced that having data at phase transitions provides better identifiability of the individual electrode parameters. The error goes down as the electrodes go through the phase transitions. It is noted that the results agree with the long-established method, Differential Voltage Analysis (DVA),

which depends on terminal voltage data across phase transitions to compute the shifts of the peak locations in the dV/dQ curve [31].

Furthermore, the results indicate that the parameters are unobservable at low DOD regions. However, in practice, compared to the simple model used in this study, there are more non-linearities near the low DODs which results in better-conditioned sensitivity matrices. Hence, the observability of the parameters should enhance in practice.

6.2. Observability of the different parameters

Recall that the problem (P) includes an equality constraint (maximum voltage limit) which intrinsically couples the error estimates of parameters x_{100} and y_{100}. Using the Taylor series expansion of the voltage constraint about the true solution the following equation is obtained

$$\sigma_y \frac{\partial U_p}{\partial y}|_{y_{100}} = \sigma_x \frac{\partial U_n}{\partial x}|_{x_{100}}. \tag{41}$$

Comparing the voltage only measurements results of x_{100} with y_{100}, it is evident that the error for x_{100} is larger than y_{100}. The reason for this disparity in estimating x_{100} and y_{100} can be explained using Eq. (41). It is apparent that $\frac{\partial U_n}{\partial x}$ at flat region of U_n is smaller than $\frac{\partial U_p}{\partial y}$ which is at the higher derivative region of U_p. Since the estimation error of x_{100} and y_{100} are proportional through Eq. (41), it stands to reason that x_{100} has larger estimation error than y_{100}.

The parameter error of C_n and C_p can also be explained by the same analysis of the sensitivity matrix. The parameter error of C_n and C_p are related to the third and fourth column of the sensitivity matrix in Eq. (38). For C_p to have a lower parameter error the window should include at least one of the asymptotes of U_p function i.e. at least two different slopes. Thus, the reason parameter error of C_p is small near the edges of fully discharged states. The same analysis is also true for C_n. As the U_n function is almost flat until high DODs.

6.3. Observability with the addition of expansion

From the results in Fig. 8, it can be seen that with the addition of expansion measurement the estimation error decreases for all the parameters. This reduction is more significant for the negative electrode parameters (x_{100}, C_n) than the positive electrode parameters (y_{100}, C_p). The reasons are that in the case of graphite/LFP cell; first, the slopes of $\Delta\mathscr{V}_{p/n}$ functions are a magnitude larger than the slopes of $U_{p/n}$ functions. Second, graphite has several rate changes while expanding, whereas LFP expands at a constant rate. As a result, the expansion is more sensitive to a change in parameters compare to voltage, especially in the middle SOC region (see Fig. 2). Hence, in this chemistry, the expansion measurement is more beneficial for the negative electrode than the positive electrode.

Finally, a threshold of 5% is selected as an acceptable amount of estimation error for the parameters. Using this criterion, it is evident that by having the expansion measurements the estimation is feasible at about 30% DOD. Hence, there is no need to have data near fully discharged states, which is important since battery packs are rarely discharged fully in automotive applications. Therefore, it is concluded that in order to have better confidence levels in the presence of noise and limited data, having the expansion measurement is necessary for estimating eSOH parameters.

7. Conclusion

The fundamental benefit of using cell expansion measurement for estimating electrode-specific SOH parameters, which correspond to the individual electrode capacity and the utilization window, was presented. First of all, to provide a measure of the identifiability of individual electrode parameters concerning the measurement noise, the standard error of the parameters was calculated by the constrained Cramer-Rao Bound. Furthermore, to make the analysis simpler and intuitive, the electrodes potential/expansion were approximated by the piecewise linear functions under the consideration of the phase transitions of materials.

The results of the lower bound of the estimation error of the individual electrode parameters using the constrained CRB formulation were compared for two scenarios of voltage measurement alone and voltage plus expansion measurements. The sensitivity matrix depends on the slope of the OCV and expansion curves. It was shown for the voltage only case that the measurements should be taken at a wider range of SOC spanning at least two phase transitions, in order to make all the parameters identifiable. However, the addition of expansion measurements made the parameters identifiable for shallower depth of discharges. As a result, for material like LFP with flat voltage response at middle SOC regions the estimation of the individual electrode parameters is feasible by including the expansion measurements.

The analysis here was based on a set of simplifying assumptions. The goal was to study the usefulness of the expansion measurements under limited data and the presence of noise. The conclusion is that having this additional information is not only beneficial, but it could be even necessary for better eSOH estimation techniques. In future works, the estimation of eSOH parameters with data collected from fresh and aged cells, effects of temperature, hysteresis, and the dynamics of the battery under nonzero current profile needs to be considered.

Acknowledgment

The authors would like to acknowledge the technical and financial support of the Automotive Research Center in accordance with Cooperative Agreement W56HZV-14-2-0001 U.S. Army Tank Automotive Research, Development and Engineering Center in Warren, MI. The authors would also like to thank Denise Rizzo, Matt Castanier, and Yi Ding of TARDEC. DISTRIBUTION A. Approved for public release; distribution unlimited.

References

[1] C. Grey, J. Tarascon, Sustainability and in situ monitoring in battery development, Nat. Mater. 16 (1) (2017) 45.
[2] C. Weng, Y. Cui, J. Sun, H. Peng, On-board state of health monitoring of lithium-ion batteries using incremental capacity analysis with support vector regression, J. Power Sources 235 (2013) 36–44.
[3] M. Dubarry, C. Truchot, B.Y. Liaw, Synthesize battery degradation modes via a diagnostic and prognostic model, J. Power Sources 219 (2012) 204–216 https://doi.org/10.1016/j.jpowsour.2012.07.016 http://www.sciencedirect.com/science/article/pii/S0378775312011330.
[4] P. Mohtat, F. Nezampasandarbabi, S. Mohan, J.B. Siegel, A.G. Stefanopoulou, On identifying the aging mechanisms in li-ion batteries using two points measurements, American Control Conference (ACC), 2017, IEEE, 2017, pp. 98–103.
[5] S. Lee, P. Mohtat, J.B. Siegel, A.G. Stefanopoulou, Beyond estimating battery state of health: identifiability of individual electrode capacity and utilization, 2018 Annual American Control Conference (ACC), IEEE, 2018, pp. 2288–2293.
[6] C.R. Birkl, M.R. Roberts, E. McTurk, P.G. Bruce, D.A. Howey, Degradation diagnostics for lithium ion cells, J. Power Sources 341 (2017) 373–386.
[7] D. Zhang, S. Dey, S.J. Moura, Lithium-ion battery state estimation for a single particle model with intercalation-induced stress, 2018 Annual American Control Conference (ACC), IEEE, 2018, pp. 2294–2299.
[8] X. Zhou, J.L. Stein, T. Ersal, Battery state of health monitoring by estimation of the number of cyclable li-ions, Contr. Eng. Pract. 66 (2017) 51–63 https://doi.org/10.1016/j.conengprac.2017.05.009 http://www.sciencedirect.com/science/article/pii/S0967066117301259.
[9] K.B. Hatzell, A. Sharma, H.K. Fathy, A survey of long-term health modeling, estimation, and control of lithium-ion batteries: challenges and opportunities, 2012 American Control Conference (ACC), 2012, pp. 584–591, , https://doi.org/10.1109/ACC.2012.6315578.
[10] N.A. Samad, Y. Kim, J.B. Siegel, A.G. Stefanopoulou, Battery capacity fading estimation using a force-based incremental capacity analysis, J. Electrochem. Soc. 163 (8) (2016) A1584–A1594.
[11] J. Cannarella, C.B. Arnold, State of health and charge measurements in lithium-ion batteries using mechanical stress, J. Power Sources 269 (2014) 7–14.
[12] M. Bauer, M. Wachtler, H. Stöwe, J.V. Persson, M.A. Danzer, Understanding the dilation and dilation relaxation behavior of graphite-based lithium-ion cells, J. Power Sources 317 (2016) 93–102.

[13] Z.J. Schiffer, J. Cannarella, C.B. Arnold, Strain derivatives for practical charge rate characterization of lithium ion electrodes, J. Electrochem. Soc. 163 (3) (2016) A427–A433.
[14] W.-J. Lai, M.Y. Ali, J. Pan, Mechanical behavior of representative volume elements of lithium-ion battery cells under compressive loading conditions, J. Power Sources 245 (2014) 609–623.
[15] B. Rieger, S. Schlueter, S.V. Erhard, A. Jossen, Strain propagation in lithium-ion batteries from the crystal structure to the electrode level, J. Electrochem. Soc. 163 (8) (2016) A1595–A1606.
[16] T.R. Ferguson, M.Z. Bazant, Nonequilibrium thermodynamics of porous electrodes, J. Electrochem. Soc. 159 (12) (2012) A1967–A1985.
[17] M. Winter, J.O. Besenhard, M.E. Spahr, P. Novk, Insertion electrode materials for rechargeable lithium batteries, Adv. Mater. 10 (10) (1998) 725–763, https://doi.org/10.1002/(SICI)1521-4095(199807)10:10<725::AID-ADMA725>3.0.CO;2-Z.
[18] B. Scrosati, J. Garche, Lithium batteries: status, prospects and future, J. Power Sources 195 (9) (2010) 2419–2430.
[19] N. Takami, A. Satoh, M. Hara, T. Ohsaki, Structural and kinetic characterization of lithium intercalation into carbon anodes for secondary lithium batteries, J. Electrochem. Soc. 142 (2) (1995) 371–379.
[20] A. Yamada, S.-C. Chung, K. Hinokuma, Optimized lifepo4 for lithium battery cathodes, J. Electrochem. Soc. 148 (3) (2001) A224–A229.
[21] M. Farkhondeh, M. Pritzker, M. Fowler, M. Safari, C. Delacourt, Mesoscopic modeling of li insertion in phase-separating electrode materials: application to lithium iron phosphate, Phys. Chem. Chem. Phys. 16 (41) (2014) 22555–22565.
[22] S. Flandrois, B. Simon, Carbon materials for lithium-ion rechargeable batteries, Carbon 37 (2) (1999) 165–180.
[23] A. Mukhopadhyay, B.W. Sheldon, Deformation and stress in electrode materials for li-ion batteries, Prog. Mater. Sci. 63 (2014) 58–116.
[24] S. Mohan, Y. Kim, J.B. Siegel, N.A. Samad, A.G. Stefanopoulou, A phenomenological model of bulk force in a li-ion battery pack and its application to state of charge estimation, J. Electrochem. Soc. 161 (14) (2014) A2222–A2231.
[25] Y. Qi, H. Guo, L.G. Hector, A. Timmons, Threefold increase in the youngs modulus of graphite negative electrode during lithium intercalation, J. Electrochem. Soc. 157 (5) (2010) A558–A566.
[26] P. Tang, N.A.W. Holzwarth, Electronic structure of $fepo_4$,a $lifepo_4$,nd related materials, Phys. Rev. B 68 (2003) 165107, https://doi.org/10.1103/PhysRevB.68.165107 https://link.aps.org/doi/10.1103/PhysRevB.68.165107.
[27] P. Stoica, B.C. Ng, On the cramér-rao bound under parametric constraints, IEEE Signal Process. Lett. 5 (7) (1998) 177–179.
[28] C. Jauffret, Observability and Fisher information matrix in nonlinear regression, IEEE Trans. Aerosp. Electron. Syst. 43 (2) (2007) 756–759, https://doi.org/10.1109/TAES.2007.4285368.
[29] X. Li, G. Fan, K. Pan, G. Wei, C. Zhu, G. Rizzoni, M. Canova, A physics-based fractional order model and state of energy estimation for lithium ion batteries. part i: model development and observability analysis, J. Power Sources 367 (2017) 187–201 https://doi.org/10.1016/j.jpowsour.2017.09.049 http://www.sciencedirect.com/science/article/pii/S0378775317312570.
[30] M. Safari, C. Delacourt, Modeling of a commercial graphite/lifepo4 cell, J. Electrochem. Soc. 158 (5) (2011) A562–A571.
[31] I. Bloom, A.N. Jansen, D.P. Abraham, J. Knuth, S.A. Jones, V.S. Battaglia, G.L. Henriksen, Differential voltage analyses of high-power, lithium-ion cells: 1. technique and application, J. Power Sources 139 (1) (2005) 295–303 https://doi.org/10.1016/j.jpowsour.2004.07.021 http://www.sciencedirect.com/science/article/pii/S0378775304008146.